

Deformation effects on the surface neutron densities of stable S and Ni isotopes probed by proton elastic scattering via isotopic analysis

Yoshiko Kanada-En'yo

Department of Physics, Kyoto University, Kyoto 606-8502, Japan

To extract structure information from proton elastic scattering off S isotopes at 320 MeV and Ni isotopes at $E_p = 180$ MeV, this study proposes isotopic analyses combining nuclear structure and reaction calculations. The isotonic analysis was repeated on ^{48}Ca and ^{50}Ti . The structure calculations were performed by using the spherical and deformed Relativistic Hartree–Bogoliubov (RHB) calculations, and the spherical nonrelativistic Skyrme Hartree–Fock–Bogoliubov calculations. The (p,p) reactions were calculated using the relativistic impulse approximation (RIA) assuming the theoretical densities of target nuclei. The RIA calculations using the target densities obtained by the RHB calculation, along with the density-dependent point-coupling interactions reasonably reproduced the (p,p) cross sections in the studied mass number region. The nuclear structure and (p,p) reactions were analyzed in detail; especially, the effects of deformation on the isotopic systematics of the surface densities and (p,p) cross sections were clarified. The deformation effects were found to be essential to describe the isotopic systematics of the experimental (p,p) cross sections. Overall, isotopic and isotonic analyses are useful for extracting the nuclear structure information such as nuclear deformations and single-particle features from proton scattering, enabling sensitive probing of surface densities.

I. INTRODUCTION

As a sensitive probe of surface neutron densities, proton elastic scattering has been utilized for extracting detailed density profiles determining the neutron skin thickness of nuclei. Accordingly, experimental researches of (p,p) reactions of various nuclei at intermediate energies have been performed [1–6]. Reaction analyses under the relativistic impulse approximation (RIA) have precisely determined the neutron densities from 295 MeV proton scattering data. These analyses employ density-dependent effective NN interactions [7] constructed from the original Murdock and Horowitz [8–10] (MH) model, hereafter called the “ddMH model”. The RIA+ddMH model has successfully described 295 MeV (p,p) reactions of various target nuclei, including Sn [4], Pb [5], and Ca [6] isotopes.

The (p,p) cross sections sensitively probe the surface neutron density, which is affected by structure properties such as neutron single-particle properties and nuclear deformations. Therefore, the (p,p) reactions provide useful information on these properties. A major advantage of proton elastic scattering is its higher quality data than other reactions including inelastic scattering, knock-out, and pick-up reactions. In my previous papers [11, 12], I analyzed the $\text{Pb}(p,p)$ and $\text{Sn}(p,p)$ reactions at 295 MeV, and showed that the cross sections were sensitive to single-particle occupation of the low- ℓ orbit in the major shell. For precise analyses with less model ambiguity, I then proposed an isotopic analysis method combining structure and reaction calculations for precise analyses with low model ambiguity and proved its applicability.

In the present work, I present isotopic analyses of proton elastic scattering from stable S and Ni isotopes at the incident energies $E_p = 180 \sim 320$ MeV. Apart from the magic nuclei, these nuclei are mid-shell nu-

clei and considered as deformed nuclei based on their $E2$ transition properties determined by γ rays and electron and hadron inelastic scattering data. I perform structure calculations based on the spherical and deformed Relativistic Hartree–Bogoliubov (RHB) calculations [13], and (for comparison) the spherical nonrelativistic Skyrme Hartree–Fock–Bogoliubov (SHFB) [14] calculations. The (p,p) reactions are calculated by the RIA-ddMH model assuming the theoretical densities of target nuclei. In particular, this study explores the deformation effects on isotopic systematics of the surface densities and (p,p) cross sections and thus examines the sensitivity of the (p,p) cross sections to the structure properties. The present application to stable nuclei aims to demonstrate that isotopic analyses of (p,p) cross sections at intermediate energies can extract the structure information, including nuclear deformations and single-particle features from nuclear reactions. The isotonic analysis is repeated on ^{48}Ca and ^{50}Ti at $N = 28$ to discuss the deformation effects of ^{50}Ti .

The remainder of this paper is organized as follows. The structure and reaction calculations are explained in Sec. II, and the results of S isotopes, Ni isotopes, and $N = 28$ isotones are presented in subsections III, IV, and V, respectively. A summary is given in Sec. VI.

II. METHODS OF NUCLEAR STRUCTURE AND REACTION CALCULATIONS

A. Structure calculations

To calculate the structures of the even–even nuclei, the spherical and deformed RHB calculations were executed in computational DIRHB code [13] with the density-dependent point-coupling (DD-PC1) (pc1) [15] and density-dependent meson-exchange

(DD-ME2) (me2) [16] interactions. In addition, the spherical SHFB was executed in HFBRAD code [14] with SKM* [17] and SLy4 [18] interactions employing mixed-type pairing forces.

B. Calculations of proton elastic scattering reactions

The proton elastic scattering at $E_p = 180 \sim 320$ MeV was calculated using the RIA+ddMH model [7]. The nucleon–nucleus potentials were obtained by folding the vector and scalar densities of target nuclei obtained by the structure calculations as described in my previous papers [11, 12]. The neutron (proton) vector densities were assumed as the theoretical neutron (proton) densities, $\rho_n(r)$ ($\rho_p(r)$) and the neutron (proton) scalar densities were set to $0.96\rho_n(r)$ ($0.96\rho_p(r)$). The same scalar densities were used in analyses of the Sn(p, p) and Pb(p, p) reactions (see Refs. [4, 5]).

The effective NN interactions in the RIA+ddMH model are based on the meson-exchange model, which includes the density dependences of the σ - and ω -meson masses and coupling constants [4, 5, 7]. These density dependences are extensions of the density-independent interactions in the original Murdock and Horowitz model [8–10]. The present RIA+ddMH calculations of the (p, p) reactions at $E_p = 180 \sim 320$ MeV adopt the latest parameterization, which has been calibrated to fit the $^{58}\text{Ni}(p, p)$ data at 295 MeV [5].

III. RESULTS OF S ISOTOPES

A. Structure properties around ^{32}S

The structures of the Si and S isotopes were calculated by the spherical and deformed RHB calculations with pc1 and me2 interactions. Figure 1 shows the β dependences of the energies of Si and S isotopes (panels (a) and (b), respectively), the neutron and proton single-particle energies and occupation probabilities in ^{34}S calculated using the pc1 interaction (panels (c) and (d), respectively), and the pairing energies in ^{32}S and ^{34}S (panels (e) and (f), respectively). As shown in the energy curves, the Si and S isotopes around ^{32}S are mid-shell nuclei that favor nuclear deformation. At the energy minima, ^{28}Si and ^{30}Si are oblatelike because of the $Z = 14$ shell effect, whereas the deformations of ^{32}S , ^{34}S , and ^{36}S change from prolate to oblate to oblate as the neutron number increases. The prolate deformation of ^{32}S is due to the single-particle energy gap between $1/2[211]$ and $1/2[200]$ orbits, whereas the oblate deformation of ^{34}S can be attributed to the energy gap between the neutron $1/2[202]$ and $1/2[200]$ orbits. ^{36}S is spherical due to the $N = 20$ shell effect. The minimum-energy states of S and Si isotopes obtained by the deformed pc1(me2)

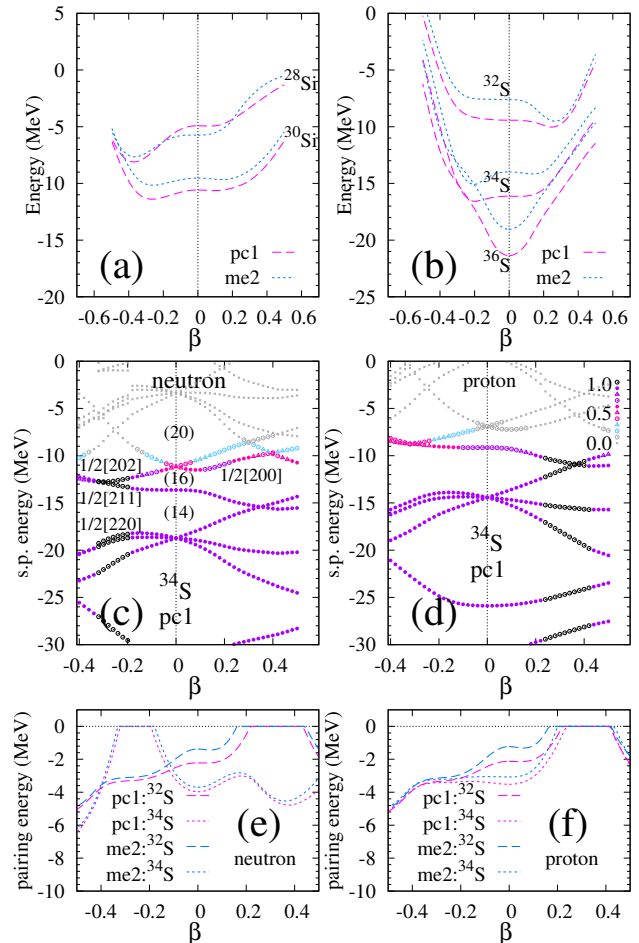


FIG. 1. Energy curves, single-particle energies, and pairing energies of Si and S isotopes obtained by the deformed RHB calculations with the pc1 and me2 interactions. Energy curves of (a) Si isotopes and (b) S isotopes; (c) neutron and (d) proton single-particle energies in ^{34}S calculated using the pc1 interaction (symbol colors indicate the occupation probabilities). (e) Neutron and (f) proton pairing energies in ^{32}S and ^{34}S .

calculations are here labeled “pc-def(me2-def)” and the spherical states at $\beta = 0$ are called “pc-sph(me2-sph)”.

The neutron and proton radii of S isotopes in the pc1-def, me2-def, pc1-sph, and me2-sph states are presented in Fig. 2, together with the experimental proton radii obtained from the charge radii. The spherical states yield slightly smaller radii than the deformed states, but both states depend similarly on N . The theoretical proton radii of the deformed and spherical states reasonably agree with the experimental data of ^{32}S , ^{34}S , and ^{36}S .

The calculated neutron densities ρ_n of the pc1-def and me2-def states of S isotopes are presented in Fig. 3(a) and the calculated $4\pi r^2 \rho_n(r)$ are drawn in Fig. 3(b). Panels (c) and (d) of this figure display the theoretical and experimental charge densities of ρ_{ch} of ^{32}S and ^{34}S , respectively. The pc1-def result well agrees with experimental charge densities of the S isotopes.

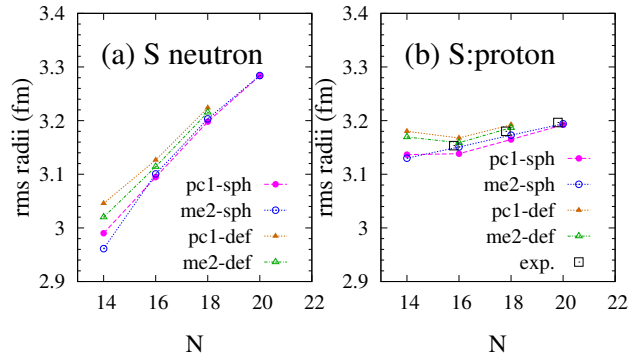


FIG. 2. Root-mean-square (rms) (a)neutron and (b) proton radii of S isotopes in the pc1-def and me2-def states for the deformed cases and in the pc1-sph and me2-sph states for the spherical cases obtained by RHB calculations. Also plotted are the experimental rms proton radii evaluated from the rms charge radii [19].

Panels (e) and (f) of Fig. 3 compare the neutron densities of the deformed and spherical states. The internal neutron densities of the pc1-def, me2-def, pc1-sph, and me2-sph scenarios visibly differ in the $r \lesssim 2$ region. In ^{32}S , the internal neutron densities are enhanced in the spherical states pc1-sph and me2-sph, where there is significant $1s_{1/2}$ occupation, but are quenched in the deformed states pc1-def and me2-def because prolate deformation decreases the $1s_{1/2}$ occupation. In the deformed case, the $1s_{1/2}$ component mixes in the $1/2[200]$ orbit above the Fermi level. The central neutron density is lowest in the me2-def state because the pairing gap vanishes in deformed ^{32}S at $\beta = 0.20$. These single-particle properties contribute to the surface neutron densities in $r \gtrsim 3$ fm, although the surface neutron densities of the deformed and spherical states show no obvious differences in the figures. In ^{34}S , the difference in central neutron density between the spherical and deformed states is smaller than in ^{32}S . Note that the proton scattering at $E \sim 300$ MeV is sensitive to surface neutron density but not to internal density.

1. Proton scattering and isotopic analysis of S isotopes

The (p, p) reactions of ^{32}S , ^{34}S , and ^{36}S at 318 MeV were calculated within the RIA+ddMH model employing the pc1-def and me2-def densities of the deformed states obtained by the RHB calculations. The calculated cross sections are compared with the experimental data in Fig. 4. The pc1-def and me2-def results are consistent with the experimental data. The results of the spherical calculations are qualitatively similar to the deformed calculations. To thoroughly investigate the deformation effect on the (p, p) cross sections, I perform isotopic analyses of the densities and cross sections of the S isotopes and compare the results of the deformed and spherical states.

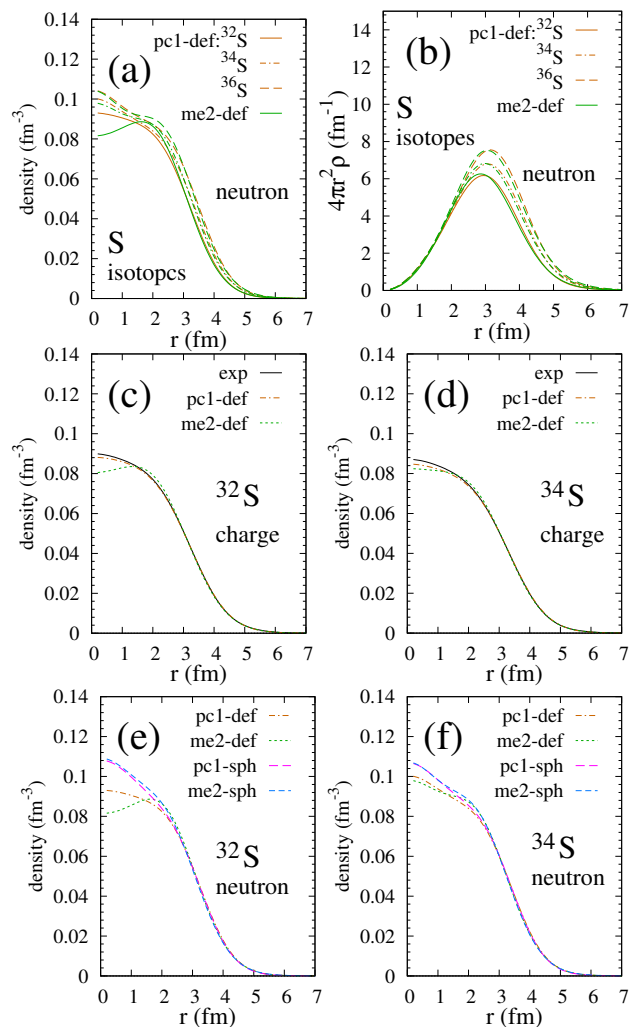


FIG. 3. Densities of S isotopes obtained in the deformed pc1 and me2 calculations: (a) neutron densities $\rho_n(r)$ and (b) $4\pi r^2 \rho_n(r)$ of S isotopes, charge densities of (c) ^{32}S and (d) ^{34}S in the pc1-def and me2-def states, together with the experimental charge densities; neutron densities of (e) ^{32}S and (f) ^{34}S for the pc1-def, me2-def, pc1-sph, and me2-sph states. The experimental charge densities were obtained from the sum-of-Gaussian (SOG) fitting parameters listed in Ref. [20].

The isotopic density differences from those of ^{32}S are defined as

$$D(\rho_n; r) \equiv \rho_n(^A\text{S}; r) - \rho_n(^{32}\text{S}; r), \quad (1)$$

$$D(\rho_{\text{ch}}; r) \equiv \rho_{\text{ch}}(^A\text{S}; r) - \rho_{\text{ch}}(^{32}\text{S}; r), \quad (2)$$

and the isotopic cross section ratios to ^{32}S are defined as

$$R(\sigma; \theta_{\text{c.m.}}) \equiv \frac{d\sigma(^A\text{S})/d\Omega}{d\sigma(^{32}\text{S})/d\Omega}. \quad (3)$$

The calculated isotopic density differences and cross section ratios are compared with the experimental values

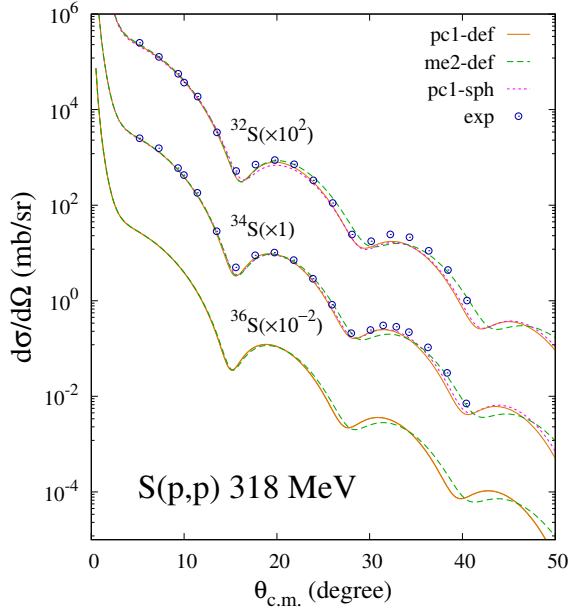


FIG. 4. $^A\text{S}(p,p)$ cross sections at 318 MeV calculated by the RIA-ddMH employing the pc1-def, me2-def, and pc1-sph densities of S isotopes. The experimental cross sections from Ref. [21] are plotted for comparison.

in Figs. 5 and 6, respectively. The pc1-def and me2-def results of $4\pi r^2 D(\rho_{\text{ch}})$ for the deformed states agree with the experimental $^{34}\text{S} - ^{32}\text{S}$ and $^{36}\text{S} - ^{32}\text{S}$ differences, but the pc1-sph and me2-sph results for the spherical states disagree with the experimental differences. In $4\pi r^2 D(\rho_n)$ plots of the neutron density, one can clearly distinguish the model dependence of the surface neutron densities around $r \sim 3$ fm between deformed and spherical states. $4\pi r^2 D(\rho_n)$ are slightly suppressed in the pc1-def and me2-def results of the deformed states because the deformation affects the single-particle orbits and occupations at the Fermi level, mainly in ^{32}S as described previously. In the spherical states, the $1s_{1/2}$ orbit is almost occupied in ^{32}S and the additional two neutrons in ^{34}S dominantly occupy the $0d_{3/2}$ orbit, so $4\pi r^2 D(\rho_n)$ increases in the $r \sim 3$ region. However, in the deformed case, the $1s_{1/2}$ component is mixed in the $1/2[200]$ orbit and partially unoccupied in the prolate ^{32}S state. Therefore, the $1s_{1/2}$ component is partially occupied by the additional two neutrons in the oblate ^{34}S state. Consequently, the $0d_{3/2}$ contribution to the $^{34}\text{S} - ^{32}\text{S}$ difference slightly decreases and $4\pi r^2 D(\rho_n)$ in the $r \sim 3$ region is decreased to some extent. This deformation effect on the isotopic difference $4\pi r^2 D(\rho_n)$ of the surface neutron densities can be sensitively probed by the (p,p) cross sections in the isotopic cross section ratios $R(\sigma)$ presented in Fig. 6. In the calculations with the deformed states (pc1-def and me2-def), the peak $R(\sigma)$ amplitudes are smaller than in the calculations with the spherical states (pc1-sph and me2-sph), because $4\pi r^2 D(\rho_n)$ around $r \sim 3$ fm is smaller

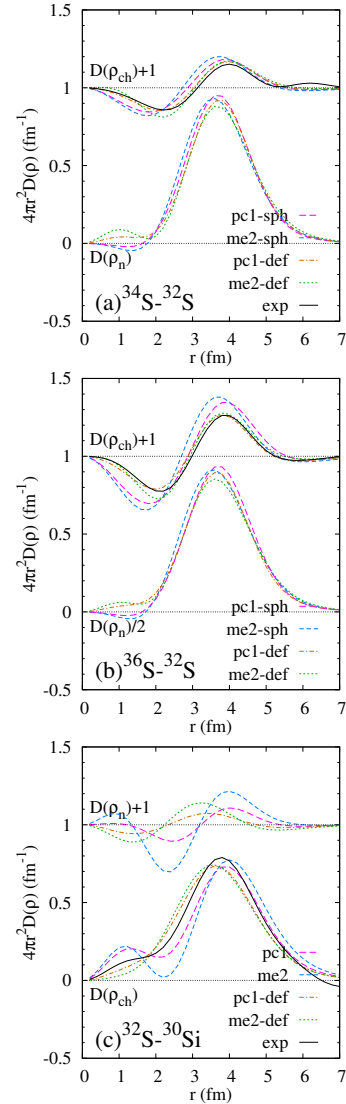


FIG. 5. Neutron and charge density differences in the pc1-def and me2-def states of S and Si isotopes obtained by the deformed RHB calculations, compared with those of the spherical states (pc1-sph and me2-sph): (a) $^{34}\text{S} - ^{32}\text{S}$ (b) $^{36}\text{S} - ^{32}\text{S}$, and (c) $^{32}\text{S} - ^{30}\text{Si}$. The experimental charge density differences obtained from Ref. [20] are also presented. $4\pi r^2 D_n(r)$ and $4\pi r^2 D_{\text{ch}}(r) + 1$ are plotted in panels (a) and (b), and $4\pi r^2 D_{\text{ch}}(r)$ and $4\pi r^2 D_n(r) + 1$ are plotted in panel (c).

than in the spherical states. The calculated $^{34}\text{S}/^{32}\text{S}$ cross section ratios more closely match the experimental $R(\sigma)$ data in the pc1-def and me2-def states than the pc1-sph and me2-sph states, indicating that deformations of the ^{32}S and ^{34}S structures are essential for describing the isotopic systematics of (p,p) cross sections.

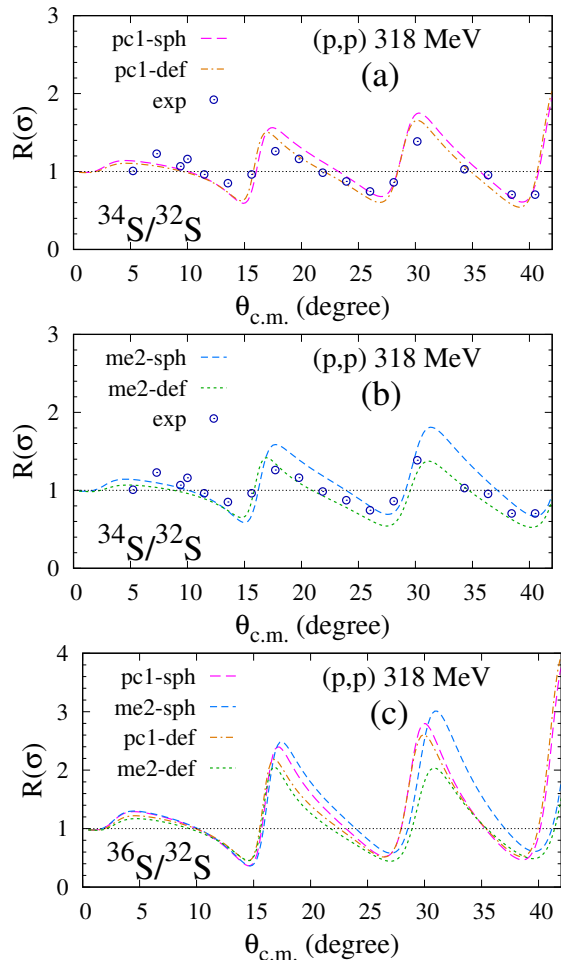


FIG. 6. Isotopic cross section ratios $R(\Omega)$ of the $^{34}\text{S}/^{32}\text{S}$ ratios of the $^A\text{S}(p,p)$ reactions at 318 MeV obtained by the RIA-ddMH calculations employing (a) pc1-def and pc1-sph and (b) me2-def and me2-sph densities. The experimental values obtained from the cross section data of Ref. [21] are plotted for comparison. (c) $R(\Omega)$ for the $^{36}\text{S}/^{32}\text{S}$ cross section ratios of 318 MeV (p,p) reaction.

IV. RESULTS OF NI ISOTOPES AROUND $N = 32$

A. Structure properties of Ni isotopes

For structure calculations of Ni isotopes, I implemented the spherical and deformed RHB models with the pc1 and me2 interactions and (for comparison) the spherical SHFB models with SKM* and SLy4 interactions. The root-mean-square neutron (r_n) and proton (r_p) radii obtained in the spherical RHB and SHFB calculations are presented in Fig. 7. The spherical pc1, me2, SKM*, and SLy4 calculations yield qualitatively similar N dependences of r_n and r_p . The N dependence of the calculated r_p deviates from the data. In particular, the SKM* and SLy4 results exhibit a kink at $N = 32$ due

to the shell effect, whereas the r_p from $^{58}\text{Ni}(N = 30)$ to $^{60}\text{Ni}(N = 32)$ is enhanced in the data. The pc1 and me2 results present no kink because the $N = 32$ shell effect is smeared by the pairing effect, but they slightly underestimate the difference of r_p between $N = 30$ and $N = 32$. Nuclear deformation is necessary for describing the N dependence of r_p in Ni isotopes around $N = 32$, as discussed later.

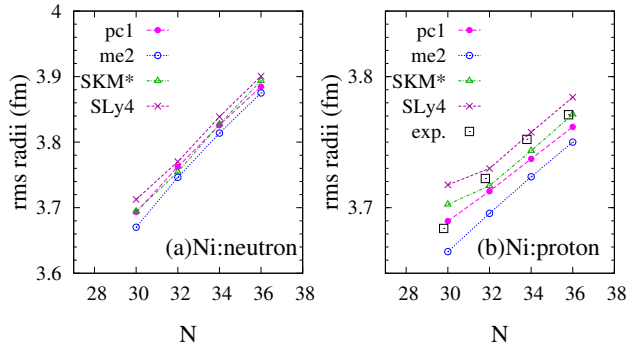


FIG. 7. Root-mean-square (rms) (a) neutron and (b) proton radii of Ni isotopes obtained in the spherical calculations of the RHB with the pc1 and me2 interactions and the SHFB with the SKM* and SLy4 interactions. The experimental rms proton radii evaluated from the rms charge radii [19] are also presented.

Figure 8 compares the experimental neutron and charge densities of ^{58}Ni with those obtained in the spherical RHB and SHFB calculations. The pc1, SKM*, and SLy4 calculations reasonably reproduce the experimental charge density at the nuclear surface in the $r = 3 \sim 5$ fm region. The pc1 calculation best match the detailed profile of $4\pi r^2 \rho_{\text{ch}}$ around the surface peak. In contrast, the me2 calculation fails to reproduce the surface charge density of ^{58}Ni .

Figure 9 plots the neutron single-particle energies and occupation probabilities in the Ni isotopes obtained by the spherical pc1 and SKM* calculations. In the pc1 result, the major shell orbits $1p_{3/2}$, $0f_{5/2}$, and $1p_{1/2}$ are almost degenerate, so the occupations of these orbits gradually increase along the isotope chain from ^{56}Ni to ^{64}Ni due to the pairing effect. The features of the single-particle properties are quite different in the SKM* results. The $1p_{3/2}-0f_{5/2}$ energy gap in this calculation reached $1 \sim 2$ MeV; accordingly, the neutron pairing gap vanishes in ^{58}Ni and ^{60}Ni . This shell effect produces the kink of r_p at $N = 32$ in the SKM* result, as mentioned previously. It should be commented that the $N = 32$ closure in ^{60}Ni is inconsistent with the direct measurements of spectroscopic factors in the $^{60}\text{Ni}(p,d)^{59}\text{Ni}$ reaction [22].

Figure 10 shows the energy curves of Ni isotopes ($A = 56-64$) calculated by the deformed RHB model and the SPE in ^{60}Ni . ^{56}Ni is a double magic nucleus and favors a spherical shape. In contrast, ^{60}Ni and ^{62}Ni favor oblate shapes because an $N = 34$ shell gap exists at

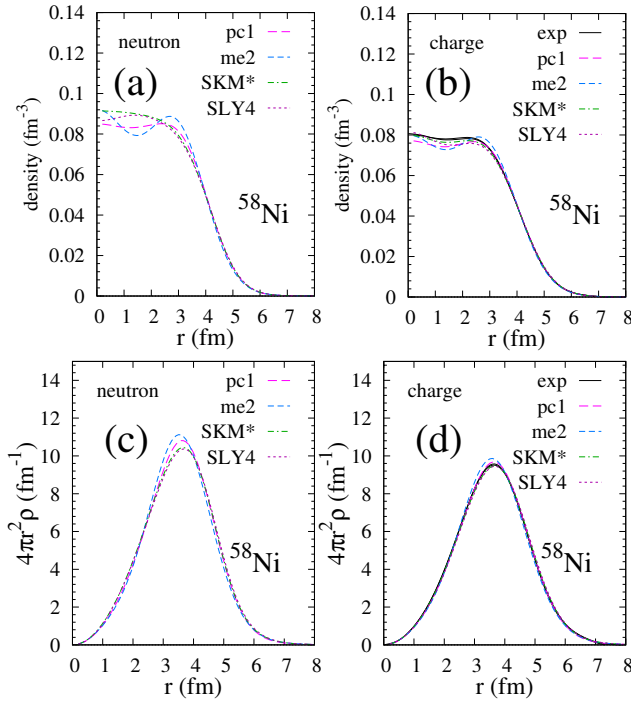


FIG. 8. Radial distributions of ^{58}Ni densities obtained in the spherical pc1, me2, SKM*, and SLY4 calculations: (a) neutron (ρ_n) and (b) charge (ρ_{ch}) densities; (c) $4\pi r^2 \rho_n(r)$; (d) $4\pi r^2 \rho_{ch}$. The experimental (exp) charge densities were obtained from the sum-of-Gaussian (SOG) fitting parameters listed in Ref. [20].

$\beta \sim -0.20$. The pc1 calculation yields minimum-energy states of ^{60}Ni (at $\beta = -0.20$) and ^{62}Ni (at $\beta = -0.23$). The energy curve of ^{58}Ni obtained by the pc1 calculation exhibits an intermediate feature. The minimum-energy state of ^{58}Ni (at $\beta = -0.08$) in this calculation shows a weak oblate deformation. However, the energy curve is almost flat in the $\beta = -0.2 \sim 0.1$ region indicating β softness of ^{58}Ni .

B. Proton scattering and isotopic analysis of Ni isotopes

The (p, p) reactions at $E_p = 178$ MeV and 295 MeV were calculated using the RIA+ddMH model with the theoretical Ni densities. Figure 11 presents the cross sections obtained using the spherical RHB calculations with pc1 and me2, together with the results of the spherical SHFB calculations with SKM* and the experimental cross sections. The pc1 result reasonably agrees with the experimental cross sections of $^{58}\text{Ni}(p, p)$ at 178 MeV and 295 MeV and $^{60}\text{Ni}(p, p)$ at 178 MeV, whereas the me2 and SKM* results deviate from the data, especially at backward angles.

The (p, p) cross sections calculated with the deformed Ni densities. The calculations with the deformed Ni

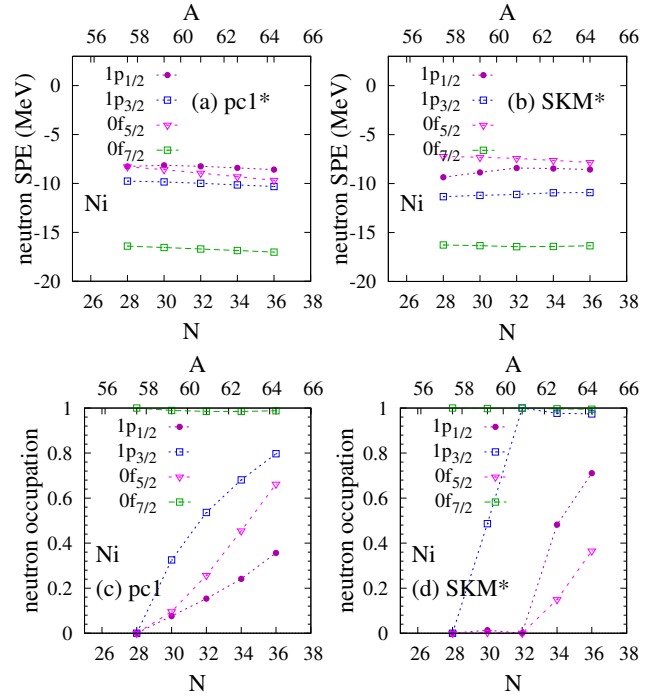


FIG. 9. (a) (b) Neutron single-particle energies and (c) (d) occupation probabilities of Ni isotopes. The results of the spherical pc1 calculations [panels (a) and (c)] and the spherical SKM* calculations [panels (b) and (d)].

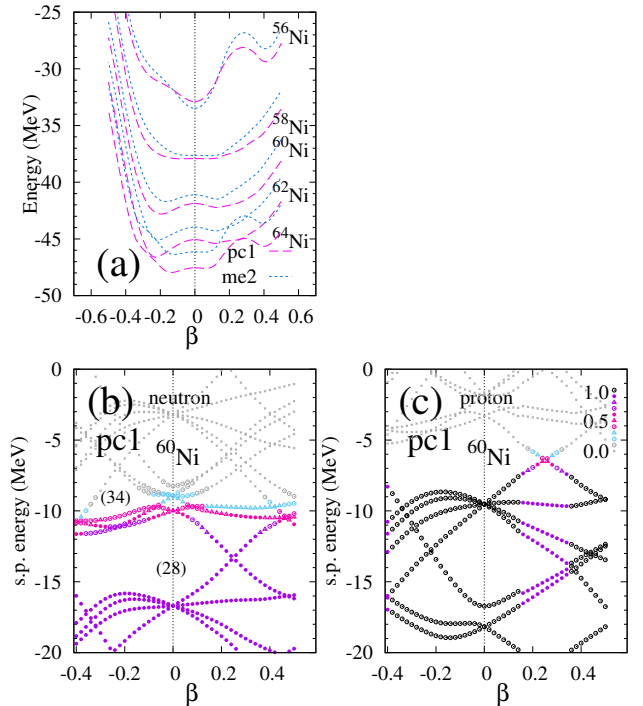


FIG. 10. (a) Energy curves of Ni isotopes obtained in the deformed RHB calculations using the pc1 and me2 interactions. (b) neutron and (c) proton single-particle energies in ^{60}Ni calculated using the pc1 interactions (symbol colors indicate the occupation probabilities).

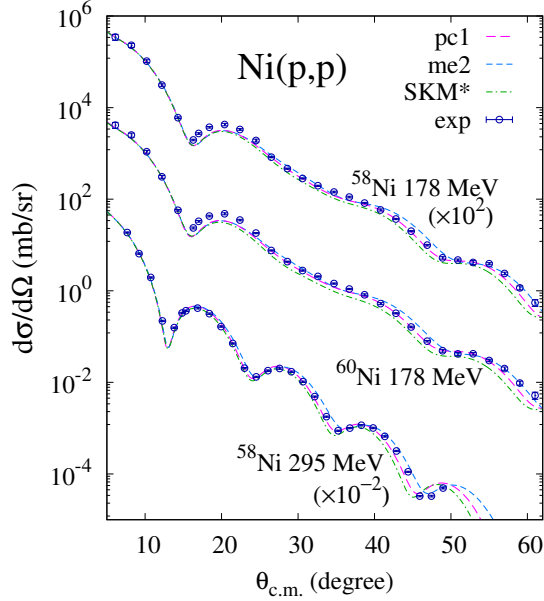


FIG. 11. $^{58}\text{Ni}(p,p)$ and $^{60}\text{Ni}(p,p)$ cross sections at 178 MeV and $^{58}\text{Ni}(p,p)$ cross sections at 295 MeV calculated by the RIA-ddMH model employing the Ni densities obtained in the spherical pc1, me2, and SKM* calculations are compared with the experimental cross sections at 178 MeV [23] and 295 MeV[5].

densities are qualitatively similar to those calculated with the spherical Ni densities. To investigate the detailed deformation effects of Ni isotopes on the (p,p) cross sections, I compared the deformed and spherical pc1 calculations in an isotopic analysis. For the deformed states of Ni isotopes, I chose the minimum-energy states obtained by the deformed pc1 calculation, namely, $^{58}\text{Ni}(\beta = -0.08)$, $^{60}\text{Ni}(\beta = -0.20)$, and $^{62}\text{Ni}(\beta = -0.23)$. This default set was named “pc1-def”. Considering the β softness of ^{58}Ni , I adopted an optional larger deformation of ^{58}Ni at $\beta = -0.17$. This optional set $\{^{58}\text{Ni}(-0.17), ^{60}\text{Ni}(-0.20), ^{62}\text{Ni}(-0.23)\}$ was named “pc1-def2”. For comparison, the spherical states at $\beta = 0$ were collected into a dataset “pc1-sph”.

Panels (a) and (b) of Fig. 12 plot the isotopic differences $D(r_p) \equiv r_p(^A\text{Ni}) - r_p(^{58}\text{Ni})$ of the r_p in the spherical and deformed states, respectively, together with the experimental values. These results reveal the N dependence of the proton radii r_p measured from r_p of ^{58}Ni . The spherical calculations underestimate $D(r_p)$ of ^{60}Ni and ^{62}Ni [Fig. 12(a)]. The pc1-def, pc1-def2, and def-sph results of the deformed states are presented in Fig. 12(b). Owing to deformation effects, the $D(r_p)$ is larger in the deformed pc results than in the spherical results. In the pc1-def result, r_p suddenly increases from $^{58}\text{Ni}(-0.08)$ to $^{60}\text{Ni}(-0.20)$ and the experimental $D(r_p)$ is overestimated at $N = 32$ and $N = 34$. In the pc1-def2 results, where the deformation changes are modest as $^{58}\text{Ni}(-0.17)$, $^{60}\text{Ni}(-0.20)$, and $^{62}\text{Ni}(-0.23)$ states,

the $D(r_p)$ values better match the experimental $D(r_p)$ at $N = 32$ and 34 than the pc1-def and pc1-sph results.

To investigate the deformation effects on the isotopic systematics of the densities and (p,p) cross sections, I calculated the isotopic density differences from ^{58}Ni

$$D(\rho_n; r) \equiv \rho_n(^A\text{Ni}; r) - \rho_n(^{58}\text{Ni}; r), \quad (4)$$

$$D(\rho_{\text{ch}}; r) \equiv \rho_{\text{ch}}(^A\text{Ni}; r) - \rho_{\text{ch}}(^{58}\text{Ni}; r), \quad (5)$$

and the isotopic cross section ratios to ^{58}Ni

$$R(\sigma; \theta_{\text{c.m.}}) \equiv \frac{d\sigma(^A\text{Ni})/d\Omega}{d\sigma(^{58}\text{Ni})/d\Omega}. \quad (6)$$

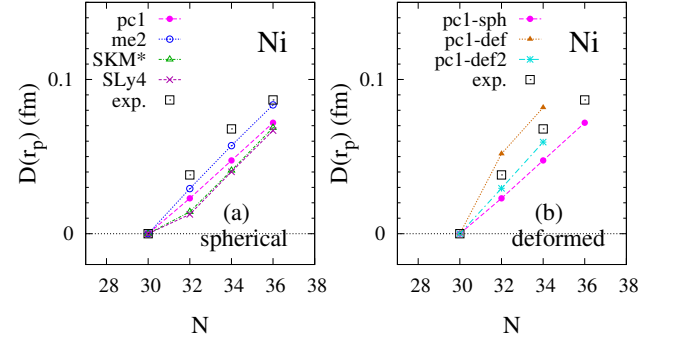


FIG. 12. (a) Isotopic differences $D(r_p) \equiv r_p(^A\text{Ni}) - r_p(^{58}\text{Ni})$ in root-mean-square proton radii from that of ^{58}Ni obtained by the spherical calculations, and (b) $D(r_p)$ of the pc1-def, pc1-def2, and pc1-sph states obtained by the deformed RHB calculations with the pc1 interaction. The experimental (exp) data were evaluated from the charge radii [19].

Panels (a) and (b) of 13 display the $4\pi r^2 D(\rho_n)$ and $4\pi r^2 D(\rho_{\text{ch}})$ obtained by the spherical pc1, me2, SKM*, and SLy4 calculations, together with the experimental $4\pi r^2 D(\rho_{\text{ch}})$. The spherical pc1 and me2 calculations slightly underestimate the positions(r) of the outer peak of $4\pi r^2 D(\rho_{\text{ch}})$, whereas the spherical SKM* and SLy4 calculations significantly underestimate the outer-peak amplitudes. The different model dependence of $D(\rho_{\text{ch}})$ in the spherical RHB (pc1 and me2) and SHFB (SKM* and SLy4) calculations can be explained by the neutron single-particle occupations. Owing to the $N = 32$ shell gap (as explained previously), the additional neutrons in ^{60}Ni and ^{62}Ni in the SKM* result [Fig. 9(d)] simply occupy the $1p_{3/2}$ orbit and only weakly change the surface proton densities, whereas in the pc1 results, the additional neutrons partially occupy the $0f_{5/2}$ orbit through the pairing effect. The $0f_{5/2}$ neutron components significantly contribute to the surface proton densities because they more strongly affect the $0f_{7/2}$ protons than the $1p_{3/2}$ neutrons. The different single-particle occupations between the pc1 and SKM* results are well-clarified in $D(\rho_n)$ [see Figs. 13(a) and (b)].

Let us discuss the deformation effects on the isotopic density differences. Panels (c) and (d) of Fig. 13 display the results of the deformed (pc1-def and pc1-def2)

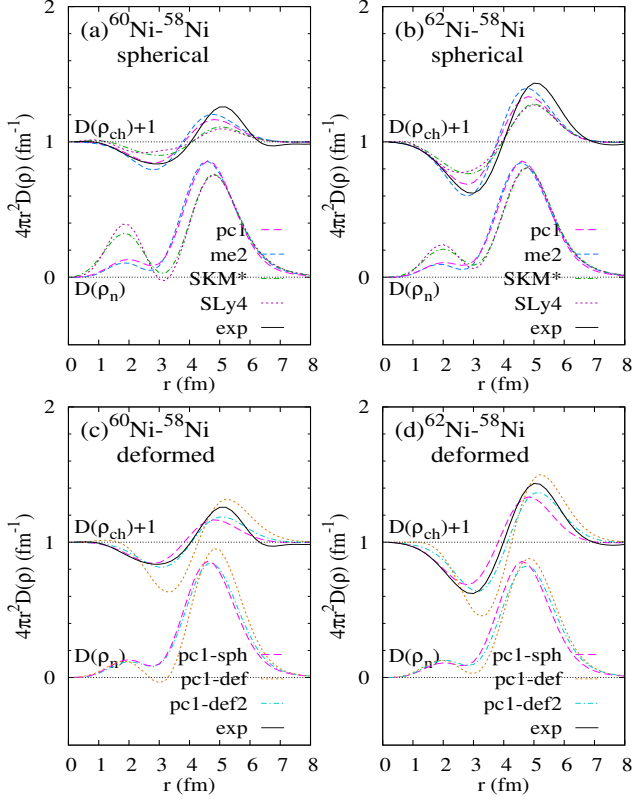


FIG. 13. Radial distributions of theoretical neutron density differences and theoretical and experimental charge density differences in Ni isotopes. (a) $^{60}\text{Ni} - ^{58}\text{Ni}$ and (b) $^{62}\text{Ni} - ^{58}\text{Ni}$ differences obtained by the spherical RHB and SHFB calculations, and (c) $^{60}\text{Ni} - ^{58}\text{Ni}$ and (d) $^{62}\text{Ni} - ^{58}\text{Ni}$ differences in the pc1-def, pc1-def2, and pc1-sph states obtained by the deformed RHB calculation. $4\pi r^2 D_n(r)$ and $4\pi r^2 D_{ch}(r) + 1$ are plotted. The experimental values were obtained from the SOG fitting parameters listed in Ref. [20].

and spherical (pc1-sph) states. The pc1-def2 (normal deformation) result of $^{58}\text{Ni}(-0.17)$ shows stronger agreement with the experimental $4\pi r^2 D(\rho_{ch})$ of both the $^{60}\text{Ni} - ^{58}\text{Ni}$ and $^{62}\text{Ni} - ^{58}\text{Ni}$ differences than the pc1-def and pc1-sph results. Meanwhile, the pc1-def (weak deformation) result of $^{58}\text{Ni}(-0.08)$ largely overestimates the data. These results suggest that a modest deformation increase around $\beta \sim -0.2$ as $^{58}\text{Ni}(-0.17)$, $^{60}\text{Ni}(-0.20)$, and $^{62}\text{Ni}(-0.23)$ is likely in the isotopic systematics of Ni isotopes.

The isotopic cross section ratio $R(\sigma)$ is sensitive to the isotopic difference $4\pi r^2 D(\rho_n)$ of the surface neutron densities around $r \sim 4$ fm. Panels (a) and (b) of Fig. 13 compare the calculated isotopic cross section ratios $R(\sigma)$ of $^{60}\text{Ni}/^{58}\text{Ni}$ at 178 MeV are compared with the experimental values. The spherical pc1 and me2 calculations reasonably agree with the experimental $R(\sigma)$, but the spherical SKM* calculation underestimates the ratios. It again excludes the $N = 32$ closure of ^{60}Ni . In the results of the deformed states [Fig.14(b)], the pc1-def2 result well re-

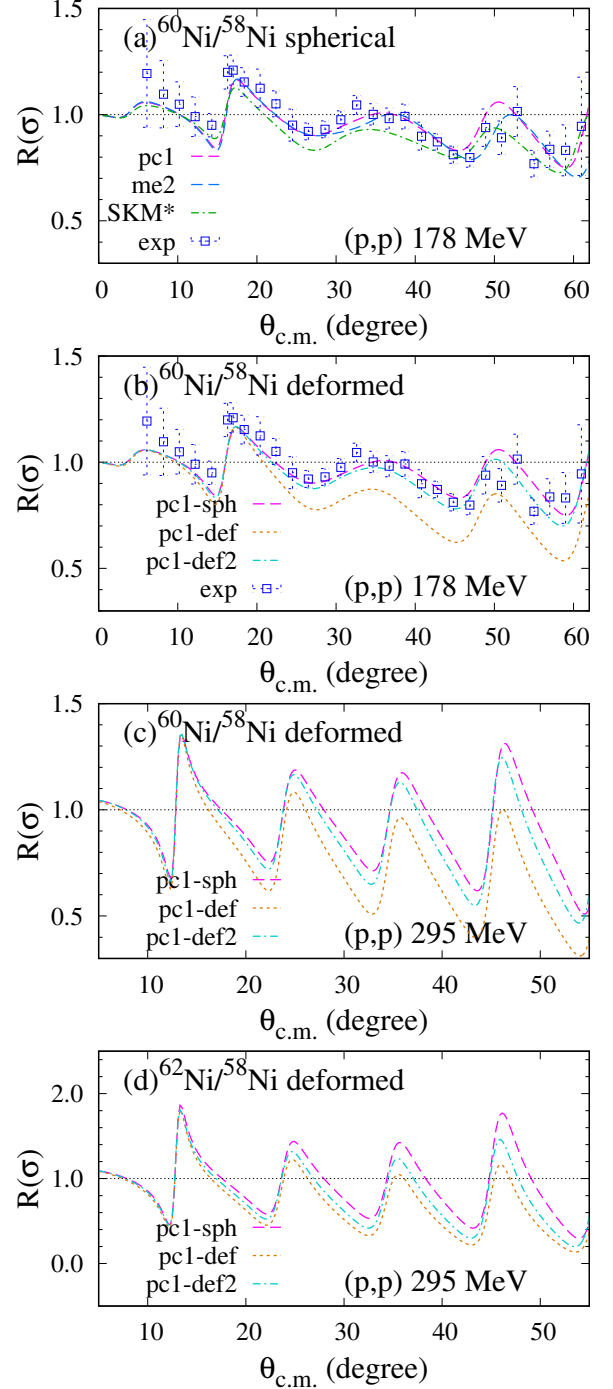


FIG. 14. Isotopic cross section ratios $R(\Omega)$ of the $(^p\text{Ni}, p)$ reactions at 178 MeV and 295 MeV obtained by the RIA-ddMH calculations employing the theoretical Ni densities, together with the experimental $R(\Omega)$ of the $(^p\text{Ni}, p)$ reactions at 178 MeV [23]. (a) $^{60}\text{Ni}/^{58}\text{Ni}$ ratios calculated using the pc1, me2, and SKM* densities obtained by the spherical calculations at 178 MeV; $^{60}\text{Ni}/^{58}\text{Ni}$ ratios (b) at 178 MeV and (c) 295 MeV and (d) $^{62}\text{Ni}/^{58}\text{Ni}$ ratios at 295 MeV calculated using the pc1-def, pc1-def2, and pc1-sph densities obtained by the deformed RHB calculations. The experimental (exp) values are the $^{60}\text{Ni}/^{58}\text{Ni}$ ratios at 178 MeV [23].

produces the experimental $R(\sigma)$, whereas the pc1-def result largely underestimates the $R(\sigma)$ amplitudes because $4\pi r^2 D(\rho_n)$ in the $r \sim 4$ fm region is smaller in pc-def than in pc1-def2 as previously described. Both the pc1-def2 and pc1-sph results reproduce the data within the experimental errors. The theoretically predicted $^{60}\text{Ni}/^{58}\text{Ni}$ and $^{62}\text{Ni}/^{58}\text{Ni}$ cross section ratios at 295 MeV are displayed in panels (c) and (d) of Fig. 13, respectively. The differences in the 295 MeV cross section ratios among the pc1-def, pc1-def2, and pc1-sph results exhibit qualitatively similar trends to the 178 MeV cross section ratios. For further analysis, high-resolution measurements of (p, p) cross sections of ^{58}Ni , ^{60}Ni , and ^{62}Ni are requested.

In the present analysis of the (p, p) reaction, the drastic deformation change from ^{58}Ni to ^{60}Ni in the pc1-def set was excluded by the experimental values of the $^{60}\text{Ni}/^{58}\text{Ni}$ cross section ratios $R(\sigma)$. Both the pc1-def2 and pc1-sph states yield reasonable $R(\sigma)$ and the better of the two cases is difficult to conclude from the existing data at 178 MeV. However, after combining the $D(\rho_{\text{ch}})$ data, it was concluded that modest deformation changes (pc1-def2: $^{58}\text{Ni}(-0.17)$, $^{60}\text{Ni}(-0.20)$, and $^{62}\text{Ni}(-0.23)$) best reproduce both the $D(\rho_{\text{ch}})$ and $R(\sigma)$ data. This result on the deformations is consistent with the quadrupole deformation parameters evaluated from the experimental $B(E2)$ values [24].

V. RESULTS OF $N = 28$ ISOTONES AROUND ^{50}Ti

As discussed in the previous sections, neutron structures such as deformations and single-particle occupations affect the detailed profile of the surface proton density. Even in proton magic $N = 28$ nuclei, the neutron deformation affects the surface proton densities as observed in the isotopic differences $D(\rho_{\text{ch}})$ data of Ni isotopes. Performing a similar analysis of the $N = 28$ isotones (^{48}Ca and ^{50}Ti), I investigated the effects of proton deformations on the surface neutron densities and demonstrated the sensitivity of proton scattering on ^{50}Ti deformation. The results are presented in the next subsection.

A. Structure properties of ^{40}Ca , ^{48}Ca , and ^{50}Ti

The structures of ^{40}Ca and ^{48}Ca , and ^{50}Ti were calculated by the spherical and deformed RHB calculations, and by the spherical SHFB calculations for comparison. The densities of ^{40}Ca and ^{48}Ca in the spherical case are presented in Fig. 15. The pc1 and me2 results are consistent with the data, but the SKM* and Sly4 results fail to reproduce the surface charge density around $r \sim 3$ fm.

The ^{40}Ca and ^{48}Ca are double magic nuclei and considered as spherical nuclei, whereas the ground band of ^{50}Ti is known as a prolate deformation with $\beta \sim 0.16$. The latter result was determined from $B(E2)$ [24] and α

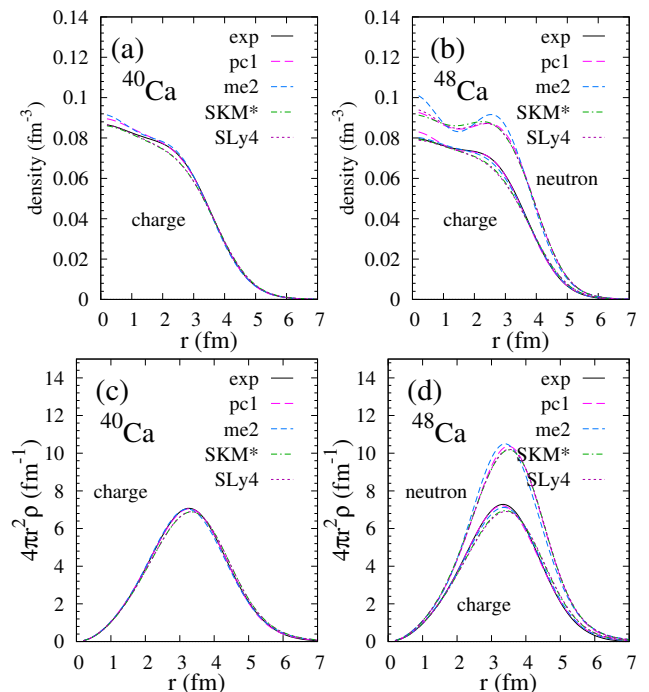


FIG. 15. Charge (ρ_{ch}) and neutron (ρ_n) densities of Ca isotopes obtained by the spherical RHB with the pc1 and me2 interactions and by the spherical SHFB with the SKM* and SLy4 interactions: (a) ρ_{ch} of ^{40}Ca , (b) ρ_{ch} and ρ_n of ^{48}Ca , (c) $4\pi r^2 \rho_{\text{ch}}$ of ^{40}Ca , and (d) $4\pi r^2 \rho_{\text{ch}}$ and ρ_n of ^{48}Ca . The experimental ρ_{ch} and $4\pi r^2 \rho_{\text{ch}}$ were obtained from the SOG fitting parameters listed in Ref. [20].

scattering [25]. The β -dependent energies obtained by the deformed pc1 and me2 calculations are presented in Fig. 16(a), and those of the neutron and proton single-particle energies of ^{50}Ti are presented in panels (b) and (c) of Fig. 16, respectively. The energy curves of ^{40}Ca (^{48}Ca) exhibit spherical energy minima caused by the $Z = 20$ and $N = 20$ ($Z = 28$) shell effects. The deformed RHB calculations of ^{50}Ti also yield spherical energy minima, although the energy curves are soft against deformation. The spherical ^{50}Ti state is inconsistent with the experimental indication of prolate deformation. To discuss the deformation effect of ^{50}Ti on the isotopic systematics of densities and (p, p) cross sections, I chose the deformed solution $^{50}\text{Ti}(\beta = 0.15)$ and compared the results of employing the spherical $^{50}\text{Ti}(\beta = 0.0)$ and deformed $^{50}\text{Ti}(\beta = 0.15)$ states.

B. Proton scattering and isotopic analysis of $N = 28$ isotones; ^{48}Ca and ^{50}Ti

The (p, p) reactions of ^{40}Ca , ^{48}Ca , and ^{50}Ti at 295 MeV were calculated using the RIA+ddMH model. Figure 17 presents the calculated cross sections obtained using the spherical pc1, me2, and SKM* calculations and the experimental data. The pc1 result agrees with the exper-

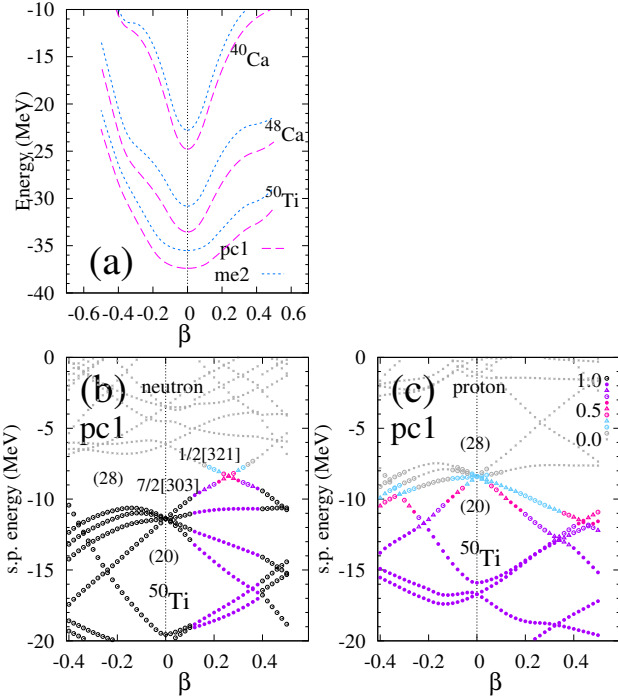


FIG. 16. (a) Energy curves of ^{40}Ca , ^{48}Ca , and ^{50}Ti obtained by the deformed RHB calculations using the pc1 and me2 interactions; (b) neutron and (c) proton single-particle energies in ^{50}Ti calculated using the pc1 interactions (symbol colors indicate the occupation probabilities).

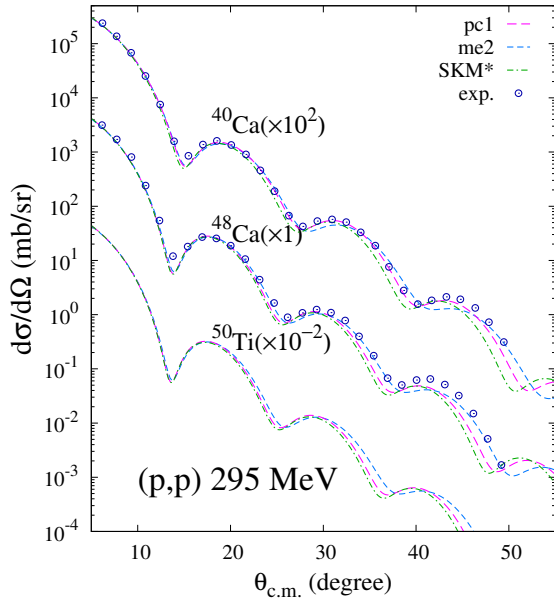


FIG. 17. $^{40}\text{Ca}(p,p)$, $^{48}\text{Ca}(p,p)$, and $^{50}\text{Ti}(p,p)$, cross sections at 295 MeV calculated by the RIA-ddMH model using the target densities obtained by the spherical pc1, me2, and SKM* calculations. Also plotted are the experimental data of the 295 MeV $^{40}\text{Ca}(p,p)$ and $^{48}\text{Ca}(p,p)$ cross sections [6].

imental $^{40}\text{Ca}(p,p)$ cross sections, whereas the me2 and SKM* results deviate from the data. For the $^{48}\text{Ca}(p,p)$ cross sections, the pc1 result reproduces the peak amplitudes of the data with a slight shift of the diffraction pattern to forward angles, whereas the me2 result underestimates the peak amplitudes at backward angles. The calculated cross sections in the pc1 and me2 results differ mainly because the surface neutron densities differ in the two interaction cases.

To investigate the sensitivity of the (p,p) cross sections to the detailed surface neutron density profile, I investigated the isotonic density differences; between ^{48}Ca and ^{50}Ti

$$D(\rho_n; r) \equiv \rho_n(^{50}\text{Ti}; r) - \rho_n(^{48}\text{Ca}; r), \quad (7)$$

$$D(\rho_{ch}; r) \equiv \rho_{ch}(^{50}\text{Ti}; r) - \rho_{ch}(^{48}\text{Ca}; r), \quad (8)$$

which are presented in Fig. 18, and the isotonic cross section ratios

$$R(\sigma; \theta_{c.m.}) \equiv \frac{d\sigma(^{50}\text{Ti})/d\Omega}{d\sigma(^{48}\text{Ca})/d\Omega}. \quad (9)$$

The results are presented in Figs. 18 and 19, respectively.

None of the spherical calculations can reproduce the experimentally observed charge density differences ρ_{ch} [Fig. 18(a)]. In all cases, the peak position of $4\pi r^2 D(\rho_{ch})$ is shifted inward relative to the experimental data. The spherical calculation results are significantly improved by employing the deformed state of ^{50}Ti ($\beta = 0.15$). The outer-region peaks in the $4\pi r^2 D(\rho_{ch})$ profiles of the ^{48}Ca ($\beta = 0.0$) and ^{50}Ti ($\beta = 0.15$) states are consistent with the experimental results [Fig. 18(b)]. Under deformation of ^{50}Ti , the neutron density difference $D(\rho_n)$ dramatically changes from the spherical case, reflecting a change in neutron single-particle properties. As shown in the neutron single-particle energies [Fig. 16(c)], prolate deformation accompanies an energy decrease of the 1/2[321] orbit from the original $1p_{3/2}$ orbit and quenching of the $N = 28$ shell gap. As a result, the pairing effect imparts a significant $1p_{3/2}$ neutron component to the deformed state ^{50}Ti ($\beta = 0.15$). This behavior explains the decreased $4\pi r^2 D(\rho_n)$ of the surface neutron densities around $r = 3 \sim 4$ fm in Fig. 18(b).

This decrease of $4\pi r^2 D(\rho_n)$ at the nuclear surface apparently contributes to the $^{50}\text{Ti}/^{48}\text{Ca}$ ratios $R(\sigma)$ of the (p,p) cross sections. Owing to the abovementioned deformation effects on the surface neutron densities, the predicted $R(\sigma)$ values obtained using the ^{50}Ti ($\beta = 0.15$) densities are significantly smaller than those of the spherical state ^{50}Ti ($\beta = 0$) [Fig. 19(a)].

To check the ambiguity among the structure calculations for $R(\sigma)$ predictions, I performed similar isotonic analyses of the densities and cross sections in the spherical ^{50}Ti ($\beta = 0.0$) and deformed ^{50}Ti ($\beta = 0.15$) states obtained by the deformed me2 calculations. The me2 results of the density differences and cross section ratios are presented in panels 18, respectively. The me2 results are qualitatively consistent with the pc1 results, although

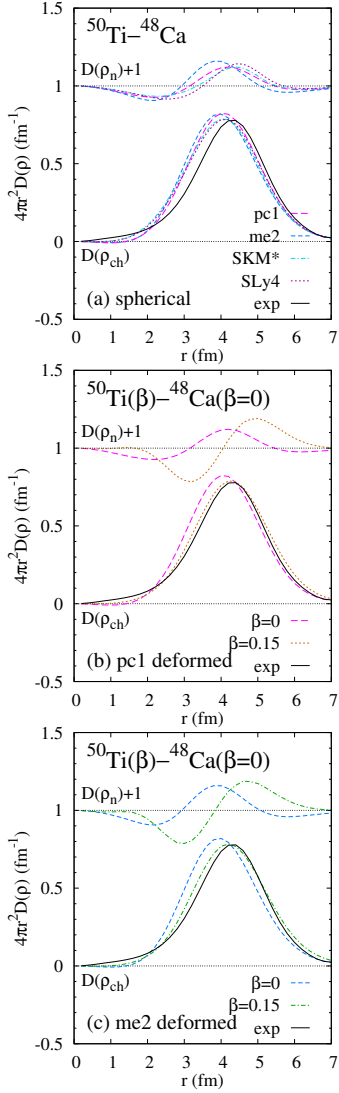


FIG. 18. Theoretical neutron and charge density differences between ^{50}Ti and ^{48}Ca , together with the experimental charge density differences: (a) density differences obtained by the spherical pc1, me2, SKM*, and SLy4 calculations; density differences between $^{50}\text{Ti}(\beta = 0.15)$ and $^{48}\text{Ca}(\beta = 0)$ states obtained by the deformed RHB calculations with the (b) pc1 and (c) me2 interactions, in comparison with those between $^{50}\text{Ti}(\beta = 0)$ and $^{48}\text{Ca}(\beta = 0)$. $4\pi r^2 D_{\text{ch}}(r)$ and $4\pi r^2 D_n(r) + 1$ are plotted. The experimental values were obtained from the SOG fitting parameters listed in Ref. [20].

the ^{48}Ca density and the $^{48}\text{Ca}(p, p)$ cross sections exhibit different features in the pc1 and me2 calculations as discussed previously. This result indicates that the present isotonic analysis can observe the ^{50}Ti deformation effect on the (p, p) cross sections while lowering the model ambiguity of the structure calculations.

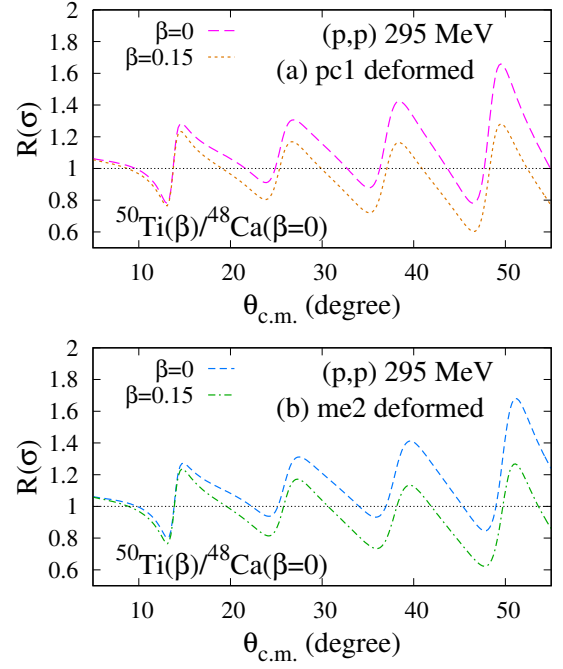


FIG. 19. Isotonic $^{50}\text{Ti}/^{48}\text{Ca}$ cross section ratios $R(\Omega)$ of (p, p) reaction at 295 MeV calculated by the RIA-ddMH model using theoretical densities obtained by the deformed RHB calculations with the (a) pc1 and (b) me2 interactions. The results obtained using the $^{48}\text{Ca}(\beta = 0)$ and $^{50}\text{Ti}(\beta = 0.15)$ densities are compared with those obtained using the $^{48}\text{Ca}(\beta = 0)$ and $^{50}\text{Ti}(\beta = 0.0)$ densities.

VI. SUMMARY

This study aimed to extract structure information from the proton elastic scattering off S isotopes at 320 MeV and Ni isotopes at $E_p = 180$ MeV. To this end, isotopic analyses were performed by combining the nuclear structure and reaction calculations and (for comparison) spherical SHFB calculations. The (p, p) reactions at intermediate energies ($E_p = 180 \sim 320$ MeV) were calculated using the RIA+ddMH model assuming the theoretical densities of the target nuclei. The RHB calculations with the pc1 interactions reasonably reproduced the experimental data of the charge densities and (p, p) cross sections in this mass number region, providing detailed analyses of the nuclear structure and (p, p) reactions. Particular attention was paid to the deformation effects on the isotopic systematics of the nuclear structures and (p, p) reactions.

The analysis of S isotopes proved that the surface neutron density can be sensitively probed by the (p, p) cross sections via isotopic analysis. The observed isotopic cross section ratios $R(\sigma)$ of 318 MeV proton scattering were better matched by the deformed RHB calculations than by the spherical RHB calculations, confirming that deformations in ^{32}S and ^{34}S are essential for replicating the

experimental data.

In the isotopic analysis of Ni isotopes, modest changes in oblate deformations in ^{58}Ni , ^{60}Ni , and ^{62}Ni most acceptably described the experimental isotopic charge density differences $D(\rho_{\text{ch}})$ and the cross section ratios $R(\sigma)$ of 178 MeV proton scattering. These deformations are consistent with the quadrupole deformation parameters evaluated from the experimental $B(E2)$.

Furthermore, I performed an isotonic analysis of the $N = 28$ isotones ^{48}Ca and ^{50}Ti , and discussed the deformation effect of ^{50}Ti on the neutron structure and (p, p) cross sections. The deformation effect of ^{50}Ti caused a significant decrease in the $^{50}\text{Ti}/^{48}\text{Ca}$ cross section ratios $R(\sigma)$.

Overall, deformation effects are essential for describing the isotopic systematics of the experimental (p, p) cross

sections. Combining the structure and reaction calculations in isotopic and isotonic analyses of the (p, p) cross sections is a useful approach for extracting nuclear structure information such as deformations and single-particle features from proton elastic scattering data at intermediate energies.

ACKNOWLEDGMENTS

This work was supported by Grants-in-Aid of the Japan Society for the Promotion of Science (Grant Nos. JP18K03617 and 18H05407) and by a grant of a joint research project of the Research Center for Nuclear Physics at Osaka University.

-
- [1] L. Ray, W. R. Coker, and G. W. Hoffmann, Uncertainties in Neutron Densities Determined from Analysis of 0.8-GeV Polarized Proton Scattering from Nuclei, *Phys. Rev. C* **18**, 2641 (1978).
- [2] L. Ray, Neutron isotopic density differences deduced from 0.8 gev polarized proton elastic scattering, *Phys. Rev. C* **19**, 1855 (1979), [Erratum: *Phys.Rev.C* 20, 1212–1212 (1979)].
- [3] G. W. Hoffmann, L. Ray, M. Barlett, J. McGill, G. S. Adams, G. J. Igo, F. Irom, A. T. M. Wang, C. A. Whitten, R. L. Boudrie, J. F. Amann, C. Glashauser, N. M. Hintz, G. S. Kyle, and G. S. Blanpied, 0.8 gev $p+^{208}\text{Pb}$ elastic scattering and the quantity Δr_{np} , *Phys. Rev. C* **21**, 1488 (1980).
- [4] S. Terashima, H. Sakaguchi, H. Takeda, T. Ishikawa, M. Itoh, T. Kawabata, T. Murakami, M. Uchida, Y. Yasuda, M. Yosoi, J. Zenihiro, H. P. Yoshida, T. Noro, T. Ishida, S. Asaji, and T. Yonemura, Proton elastic scattering from tin isotopes at 295 mev and systematic change of neutron density distributions, *Phys. Rev. C* **77**, 024317 (2008).
- [5] J. Zenihiro, H. Sakaguchi, T. Murakami, M. Yosoi, Y. Yasuda, S. Terashima, Y. Iwao, H. Takeda, M. Itoh, H. P. Yoshida, and M. Uchida, Neutron density distributions of $^{204,206,208}\text{Pb}$ deduced via proton elastic scattering at $E_p = 295$ mev, *Phys. Rev. C* **82**, 044611 (2010).
- [6] J. Zenihiro *et al.*, Direct determination of the neutron skin thicknesses in $^{40,48}\text{Ca}$ from proton elastic scattering at $E_p = 295$ MeV, (2018), arXiv:1810.11796 [nucl-ex].
- [7] H. Sakaguchi, H. Takeda, S. Toyama, M. Itoh, A. Yamagoshi, A. Tamii, M. Yosoi, H. Akimune, I. Daito, T. Inomata, T. Noro, and Y. Hosono, Elastic scattering of polarized protons from ^{58}Ni at $E_p = 192, 295,$ and 400 mev, *Phys. Rev. C* **57**, 1749 (1998).
- [8] C. J. Horowitz, Relativistic Love-Franey model: Covariant representation of the NN interaction for N-nucleus scattering, *Phys. Rev. C* **31**, 1340 (1985).
- [9] D. P. Murdock and C. J. Horowitz, Microscopic Relativistic Description of Proton - Nucleus Scattering, *Phys. Rev. C* **35**, 1442 (1987).
- [10] C. Horowitz, D. Murdock, and S. B.D., *Computational Nuclear Physics 1*, edited by K. Lan-
- ganke, J. Maruhn, and S. Koonin (Springer-Verlag, 1991) p. 129.
- [11] Y. Kanada-En'yo, Isotopic analysis of 295 MeV proton scattering off $^{204,206,208}\text{Pb}$ for improvement of neutron densities and radii, (2021), arXiv:2106.00151 [nucl-th].
- [12] Y. Kanada-En'yo, Shell effect in $A = 116\text{--}124$ Tin isotopes investigated using isotopic analysis of proton scattering at 295 MeV, (2021), arXiv:2106.00930 [nucl-th].
- [13] T. Nikšić, N. Paar, D. Vretenar, and P. Ring, DIRHB - A relativistic self-consistent mean-field framework for atomic nuclei, *Comput. Phys. Commun.* **185**, 1808 (2014), arXiv:1403.4039 [nucl-th].
- [14] K. Bennaceur and J. Dobaczewski, Coordinate-space solution of the Skyrme-Hartree-Fock-Bogolyubov equations within spherical symmetry. The Program HFBRAD (v1.00), *Comput. Phys. Commun.* **168**, 96 (2005), arXiv:nucl-th/0501002.
- [15] T. Nikšić, D. Vretenar, and P. Ring, Relativistic Nuclear Energy Density Functionals: Adjusting parameters to binding energies, *Phys. Rev. C* **78**, 034318 (2008), arXiv:0809.1375 [nucl-th].
- [16] G. A. Lalazissis, T. Nikšić, D. Vretenar, and P. Ring, New relativistic mean-field interaction with density-dependent meson-nucleon couplings, *Phys. Rev. C* **71**, 024312 (2005).
- [17] J. Bartel, P. Quentin, M. Brack, C. Guet, and H. B. Hakansson, Towards a better parametrisation of Skyrme-like effective forces: A Critical study of the SkM force, *Nucl. Phys. A* **386**, 79 (1982).
- [18] E. Chabanat, P. Bonche, P. Haensel, J. Meyer, and R. Schaeffer, A Skyrme parametrization from subnuclear to neutron star densities. 2. Nuclei far from stabilities, *Nucl. Phys. A* **635**, 231 (1998), [Erratum: *Nucl.Phys.A* 643, 441–441 (1998)].
- [19] I. Angeli and K. P. Marinova, Table of experimental nuclear ground state charge radii: An update, *Atom. Data Nucl. Data Tabl.* **99**, 69 (2013).
- [20] H. De Vries, C. W. De Jager, and C. De Vries, Nuclear charge and magnetization density distribution parameters from elastic electron scattering, *Atom. Data Nucl. Data Tabl.* **36**, 495 (1987).
- [21] J. J. Kelly *et al.*, Neutron and proton transition densi-

- ties from S-32, S-34 (p, p') at $E_p=318$ MeV. 1. Isoscalar densities for S-32, Phys. Rev. C **44**, 1963 (1991).
- [22] M. Matoba, O. Iwamoto, Y. Uozumi, T. Sakae, N. Koori, H. Ohgaki, H. Kugimiya, H. Ijiri, T. Maki, and M. Nakano, Fragmentation of neutron-hole strengths in ^{59}Ni observed in the $^{60}\text{Ni}(p,d)^{59}\text{Ni}$ reaction at 65 MeV, Nucl. Phys. A **581**, 21 (1995).
- [23] A. Ingemarsson, T. Johansson, and G. Tibell, ELASTIC AND INELASTIC SCATTERING OF 178-MEV PROTONS FROM NI-58 AND NI-60, Nucl. Phys. A **365**, 426 (1981).
- [24] B. Pritychenko, M. Birch, B. Singh, and M. Horoi, Tables of E2 Transition Probabilities from the first 2^+ States in Even-Even Nuclei, Atom. Data Nucl. Data Tabl. **107**, 1 (2016), [Erratum: Atom.Data Nucl.Data Tabl. 114, 371–374 (2017)], arXiv:1312.5975 [nucl-th].
- [25] H. Rebel, G. Hauser, G. W. Schweimer, G. Nowicki, W. Wiesner, and D. Hartmann, The deformation of 46, 48, 50 Ti from 104 MeV α -particle scattering, Nucl. Phys. A **218**, 13 (1974).